RESEARCH ARTICLE | OCTOBER 22 2024

Synthesis of group-IV ternary and binary semiconductors using epitaxy of GeH₃Cl and SnH₄ ⊘

Aixin Zhang ⑩ ; Dhruve A. Ringwala ⑩ ; Matthew A. Mircovich ⑩ ; Manuel A. Roldan ⑩ ; John Kouvetakis ➡ ⑩ ; José Menéndez ⑩



J. Vac. Sci. Technol. A 42, 062704 (2024)

https://doi.org/10.1116/6.0003991

A CHORUS





Articles You May Be Interested In

Synthesis of short-wave infrared $Ge_{1-y}Sn_y$ semiconductors directly on Si(100) via ultralow temperature molecular routes for monolithic integration applications

J. Vac. Sci. Technol. A (November 2022)

Compositional dependence of the absorption edge and dark currents in $Ge_{1-x-y}Si_xSn_y/Ge(100)$ photodetectors grown via ultra-low-temperature epitaxy of Ge_4H_{10} , Si_4H_{10} , and SnD_4

Appl. Phys. Lett. (November 2012)

Gas source molecular epitaxy of $Ge_{1-y}Sn_y$ materials and devices using high order Ge_4H_{10} and Ge_5H_{12} hydrides

J. Vac. Sci. Technol. A (November 2021)





Synthesis of group-IV ternary and binary semiconductors using epitaxy of GeH3Cl and SnH4

Cite as: J. Vac. Sci. Technol. A 42, 062704 (2024); doi: 10.1116/6.0003991 Submitted: 16 August 2024 · Accepted: 3 October 2024 ·







Published Online: 22 October 2024

Aixin Zhang, 🛮 📵 Dhruve A. Ringwala, 🕽 📵 Matthew A. Mircovich, 🖰 📵 Manuel A. Roldan, 🕉 📵 John Kouvetakis, 🗀 📵



AFFILIATIONS

and José Menéndez² [[

- ¹School of Molecular Sciences, Arizona State University, Tempe, Arizona 85287-1604
- ²Department of Physics, Arizona State University, Tempe, Arizona 85287-1504
- Seyring Materials Center, Arizona State University, Tempe, Arizona 85287-8301

ABSTRACT

Ge_{1-x-v}Si_xSn_v alloys were grown on Ge buffers via reactions of SnH₄ and GeH₃Cl. The latter is a new CVD source designed for epitaxial development of group-IV semiconductors under low thermal budgets and CMOS-compatible conditions. The $Ge_{1-x-y}Si_xSn_y$ films were produced at very low temperatures between 160 and 200 °C with 3%-5% Si and ~5%-11% Sn. The films were characterized using an array of structural probes that include Rutherford backscattering, x-ray photoelectron spectroscopy, high-resolution x-ray diffraction, scanning transmicrostructures, flat surfaces, homogeneous compositions, and sharp interfaces. Raman was used to determine the compositional dependence of the vibrational modes indicating atomic distributions indistinguishable from those obtained when using high-order Ge hydrides. For a better understanding of the growth mechanisms, a parallel study was conducted to investigate the GeH₃Cl applicability for synthesis 8 of binary $Ge_{1-y}Sn_y$ films. These grew strained to Ge, but with reduced Sn compositions and lower thicknesses relative to $Ge_{1-x-y}Si_xSn_y$. Bypassing the Ge buffers led to Ge_{1-y}Sn_y-on-Si films with compositions and thicknesses comparable to Ge_{1-y}Sn_y-on-Ge; but their strains were mostly relaxed. Efforts to increase the concentration and thickness of $Ge_{1-\nu}Sn_{\nu}$ -on-Si resulted in multiphase materials containing large amounts of interstitial Sn. These outcomes suggest that the incorporation of even small Si amounts in $Ge_{1-x-y}Si_xSn_y$ might compensate for the large Ge-Sn mismatch by lowering bond strains. Such an effect reduces strain energy, enhances stability, promotes higher Sn incorporation, and increases critical thickness.

Published under an exclusive license by the AVS. https://doi.org/10.1116/6.0003991

I. INTRODUCTION

 $Ge_{1-\nu}Sn_{\nu}$ and $Ge_{1-x-\nu}Si_{x}Sn_{\nu}$ alloys are the latest members of the group-IV semiconductor family. They extend the optoelectronic capabilities of this family beyond the $1.5 \mu m$ Ge-threshold and well into the infrared, while maintaining compatibility with Si platforms. 1-3 Initial demonstrations of Si-Ge-Sn photodetectors with extended infrared responsivity⁴ and lasers operating at low temperature established the potential of these alloys for practical applications. However, their synthesis requires nonequilibrium routes at low temperatures, 5-8 since the materials are thermodynamically stable only at very low Sn concentrations of \sim 1%.

The original nonequilibrium approach to Si-Ge-Sn utilized a chemical vapor deposition (CVD) method based on higher-order

Ge hydrides (Ge₂H₆, Ge₃H₈, and Ge₄H₁₀) instead of the simpler GeH₄. 9-13 The choice of these heavier hydrides was motivated by their higher reactivity at low temperatures. The latter are crucial for synthesizing materials with ultrahigh Sn contents, which are essential for obtaining continuous bandgap tuning across the entire short-wave infrared (SWIR) and mid-wave infrared (MWIR) spectral ranges. 14,15 $\mathrm{Ge_{2}H_{6}}$ was employed in the first CVD synthesis of Ge_{1-v}Sn_v via reactions with SnH₄ and also in the initial demonstration of $Ge_{1-x-y}Si_xSn_y$ alloys. ^{9,10} Subsequently, Ge_2H_6 was applied to grow $Ge_{1-y}Sn_y$ using $SnCl_4$ as the source of $Sn.^{11}$ Ge_3H_8 and Ge₄H₁₀ were introduced to achieve even lower-temperature alternatives to Ge_2H_6 . $^{12,13,16-18}$ The advances enabled by Ge_3H_8 and Ge₄H₁₀ include (a) extended compositional ranges reached by lowering the growth temperature to levels not achievable with other

a)Author to whom correspondence should be addressed: Jkouvetakis@asu.edu



CVD approaches, allowing the growth of $Ge_{1-\nu}Sn_{\nu}$ and $Ge_{1-x-y}Si_xSn_y$ samples with ultrahigh Sn contents up to 36% Sn, (b) compatibility with in situ doping with full activation of dopants and extremely flat doping profiles at low temperatures, and (c) nearly full incorporation of all group-IV elements in the gas phase into the solid film, minimizing waste of Ge. The major disadvantages of the Ge₃H₈ and Ge₄H₁₀ route are the low vapor pressure of the latter (only 1 Torr at 22 °C), which may limit its practicality for large-scale industrial applications, and the fact that their synthesis requires pyrolysis of Ge₂H₆ in a flow reactor at 250 °C. This process generates significant amounts of GeH₄ secondary products. GeH₄ can be fully recovered and recycled, but the extra pyrolysis step adds to the complexity of the process and to its potential cost when exploring commercial opportunities.

The current alternative to polygermanes for CVD of Ge_{1-v}Sn_v and $Ge_{1-x-y}Si_xSn_y$ alloys is the use of GeH_4 in combination with SnCl₄ (Refs. 19-22). GeH₄ (germane) is the commonly used reagent for fabricating Ge-containing semiconductors, including Ge-on-Si platforms for photonic applications as well as Ge_{1-x}Si_x materials and devices on Si. 23,24 Due to its compatibility with commercial reactors, the GeH₄ approach to Sn-containing alloys is particularly attractive for mass-scale production. The much lower reactivity of GeH₄ relative to the higher-order Ge hydrides, as highlighted above, is accommodated by using a 100-1000 fold excess partial pressure of GeH₄. ^{19,22} Since the excess GeH₄ is wasted, the approach may become very costly if Ge prices keep increasing as in the past few years (37% so far in 2024, 96% since 2021, Ref. 25). While these dramatic price increases are linked to current geopolitical events, the long-term trend is likely to be in the same direction due to the increasing demand for Ge, the environmental concerns associated with Ge separation technologies, and the low natural abundance of this element.²⁶⁻²⁸ Furthermore, the compositions in this regime are controlled mainly by the deposition temperature rather than the more robust use of classical stoichiometry of the gaseous sources.

In order to overcome the disadvantages of the polygermane and germane synthetic routes to the growth of Ge-Si-Sn systems, we recently targeted precursors that are more easily accessible in large quantities. The goal was to find compounds with physical properties closer to GeH₄ but with improved chemical reactivity for low-temperature CVD, as is the case with the polygermanes. To this end, we produced and tested the GeH₃Cl derivative of GeH₄. The synthesis is conducted via straightforward chlorination of GeH₄ at room temperature based on the following reaction:

$$SnCl_4 + GeH_4 \rightarrow GeH_3Cl + SnCl_2 + HCl.$$
 (1)

GeH₃Cl has a much higher vapor pressure much higher than Ge₄H₁₀ (530 Torr at room temperature) while rivaling its reactivity, which up to now was considered the highest from the general family of Ge hydrides. The potential of GeH₃Cl as a CVD source was demonstrated in prior work with the deposition of device quality Ge films on Si wafers at 330-350 °C.²⁹ These films exhibited crystallinity, thickness, and morphology comparable to films produced by Ge₄H₁₀. The layers were doped with phosphorus and boron for the fabrication of photodiodes that exhibited higher responsivity and lower dark current compared to Ge₄H₁₀ analogs. In addition, it was shown that GeH₃Cl is amenable to ultralow temperature (200 °C) deposition of $Ge_{1-y}Sn_y$ films (2%Sn) on Si. These results suggested that GeH3Cl likely follows a similar dissociation pathway as Ge₄H₁₀, involving the formation of GeH₂ reactive intermediates. This was further borne out by control thermolysis experiments of GeH₃Cl. These showed that the compound undergoes homogeneous dissociation driven by HCl elimination, likely yielding GeH2 according to

$$GeH_3Cl \rightarrow GeH_2 + HCl.$$
 (2)

GeH₂ can then serve as the enabling building blocks for Ge crystal assembly at low temperatures. The high reactivity of GeH₃Cl motivated us to further develop this compound as a viable precursor for ultralow temperature synthesis of epitaxial films. In this study, we built upon our prior work on depositing pure Ge by using GeH_3Cl to synthesizing $Ge_{1-x-y}Si_xSn_y$ alloys, demonstrating the versatility of this precursor in depositing a range of Ge-based semiconductors. The Ge_{1-x-v}Si_xSn_v samples are produced via reactions of GeH₃Cl with the SnH₄ and Si₄H₁₀ sources using Ge-buffered Si platforms as substrates. The Sn contents was varied from 5% to 11% and the Si from 5% to 2.5% by reducing the temperature from 200 to 160 °C. The growth of $Ge_{1-\nu}Sn_{\nu}$ analogs was also performed under similar conditions to investigate the influence of Si incorporation on the growth properties of the binary. In this connection, we find that Si atoms in the structure facilitate higher Sn substitution. This seems to be a general characteristic of Ge_{1-x-y}Si_xSn_y CVD growth, as it was also observed for different № precursors. 30,31 The higher Sn substitution promotes larger thicknesses in epitaxial layers and induces better crystallinity. Our collective results indicate that adopting GeH₃Cl in the place of Ge₄H₁₀ as a Ge source for low-temperature processing is both feasible and 8 practical.

Notably, GeH₃Cl exhibits similar reactivity to SnH₄, as $\frac{60}{50}$ required for fabricating Sn-containing samples with tunable compositions across a wide range. A key benefit of GeH₃Cl is that, like Ge₄H₁₀, it reacts at ultralow temperatures that are compatible with the stability range of high Sn content alloys. But, GeH3Cl offers additional benefits in that it is easier to handle and less expensive to produce compared to Ge₄H_{10.}

II. EXPERIMENT

A. Growth of $Ge_{1-x-y}Si_xSn_y$ via GeH_3CI

The depositions of films were performed in a gas-source molecular epitaxy chamber (GSME) with base pressure $P = 10^{-10}$ Torr. The chamber typically operates at T < 400 °C and P in the $\sim 10^{-4}$ - 10^{-7} Torr range. Four-inch $\langle 001 \rangle$ Ge-buffered Si wafers with $0.01\,\Omega$ cm resistivity served as substrates. The buffer layers were grown at 350 °C using GeH₃Cl or Ge₄H₁₀. Their thicknesses ranged from 500 to 700 nm.

The Ge-buffered substrates were chemically cleaned in a 5% HF/H₂O bath, dried under nitrogen, and loaded into the chamber. They were then heated to 650 °C under UHV for several hours to desorb surface impurities. A glass vessel with liquid GeH3Cl was connected to one gas inlet of the injection manifold of the chamber, while another vessel containing a 10:1 mixture of SnH₄

and $\mathrm{Si_4H_{10}}$ was connected to a second inlet allowing independent control of the reactants inside the chamber. This dual arrangement ensured that the gaseous sources combined in desired proportions at the growth surface in a steady and continuous manner. $\mathrm{GeH_3Cl}$ vapor was admitted first inside the reactor, raising the pressure from 10^{-10} to $4\times10^{-5}\,\mathrm{Torr}$. Then, the $\mathrm{SnH_4}$ and $\mathrm{Si_4H_{10}}$ stock mixture was injected, further raising the pressure to a final $6\times10^{-5}\,\mathrm{Torr}$. The precurosrs were fed continuously and the working pressure was held constant during the experiments by continuous turbo pumping of the chamber contents.

A series of growth experiments was conducted under these conditions by adjusting the reaction temperature from 200 to 160 $^{\circ}$ C. While temperature was the primary variable, flux rates and reactant ratios were also adjusted to optimize crystal quality and Si/Sn stoichiometry. This approach provided insights into the reactivity behavior of GeH₃Cl with the Si and Sn sources, as well as the incorporation of Si and Sn atoms under ultralow temperatures.

Samples with mirrorlike surfaces were produced under optimized conditions and were fully characterized by Rutherford backscattering (RBS), x-ray photoelectron spectroscopy (XPS), spectroscopic ellipsometry, high-resolution x-ray diffraction (HRXRD), atomic force microscopy (AFM), scanning transmission electron microscopy (XTEM), and Raman scattering. Table I summarizes growth conditions and characterization results for representative samples including Sn/Si compositions, cubic lattice constants, strain states, and film thicknesses.

The bulk atomic concentrations of Si, Sn, and Ge were directly measured by RBS and corroborated by HRXRD. RBS was essential for determining Si concentration which XRD alone cannot provide. Figure 1(a) shows RBS spectra using He²⁺ ion energies of 2.0 MeV in a General Ionex Tandetron Accelerator. The experimental geometry to obtain random and channeled spectra as well as the method used to extract atomic concentrations from the spectra are described in detail in Ref. 32. The logarithmic scale plot provides an enlarged view of the baseline, highlighting a clearly resolved Si signal which is marked by an arrow. Strong Ge and Sn signals from the buffer and the epilayer are visible in the spectrum. The film Si signal appears as a low intensity peak adjacent to the Ge signal from the buffer layer. Model fits indicate Si and Sn contents of 4.6% Si and 6.3% Sn, respectively, and a film thickness of 100 nm,

TABLE I. Summary of $Ge_{1-x-y}Si_xSn_y$ (y = 0.055–0.11) samples grown on Ge-buffered Si(100) and corresponding growth temperature T_g , compositions, strain (ε) , relaxed lattice constant (a_0) , and thicknesses.

Sample	<i>T_g</i> (°C)	XRD Sn (%)	RBS Sn (%)	Si (%)	ε (%)	a ₀ (Å)	Thickness (nm)
1	195	5.5	5.4	5	-0.4563	5.6919	70
2	183	6.7	6.3	4.6	-0.6051	5.7024	100
3	180	7	6	4.1	-0.7038	5.706	75
4	180	6.9	6.3	3	-0.7119	5.7074	40
5	175	8.2	8.3	2.3	-0.9283	5.72	57
6	170	8.2	7.8	2.5	-0.9801	5.7215	55
7	165	9.6	9	2.5	-1.147	5.7319	34
8	160	10.7	10.7	2.5	-1.1888	5.7407	35

in agreement with ellipsometry measurements. In addition to the 2 MeV spectra, higher energy plots at 3–3.7 MeV were also measured to resolve Si peaks in cases where the samples exhibited overlapping Ge and Si signals from the buffer and the epilayer, respectively. We note that all samples were analyzed using RBS to verify the presence of distinct Si peaks, and model fits of the spectra provided the absolute Si contents listed in Table I.

In addition to the random RBS, the channeled spectra were also measured. Figure 1(b) compares the random (black line) and channeled spectra (red line) of sample 2 measured at 2 MeV. The random spectrum features a broad peak resulting from overlapping Ge signals of the epilayer and the Ge buffer, along with a narrow Sn peak from the film. The high degree of channeling indicated by the low intensity of the red signal suggests that the constituent atoms occupy the same lattice. This is consistent with the single-phase character indicated by the HXRD analysis discussed below. The classic channeling profile observed throughout this sample is characteristic of a material with excellent crystallinity, well aligned interfaces, and low-defectivity microstructure.

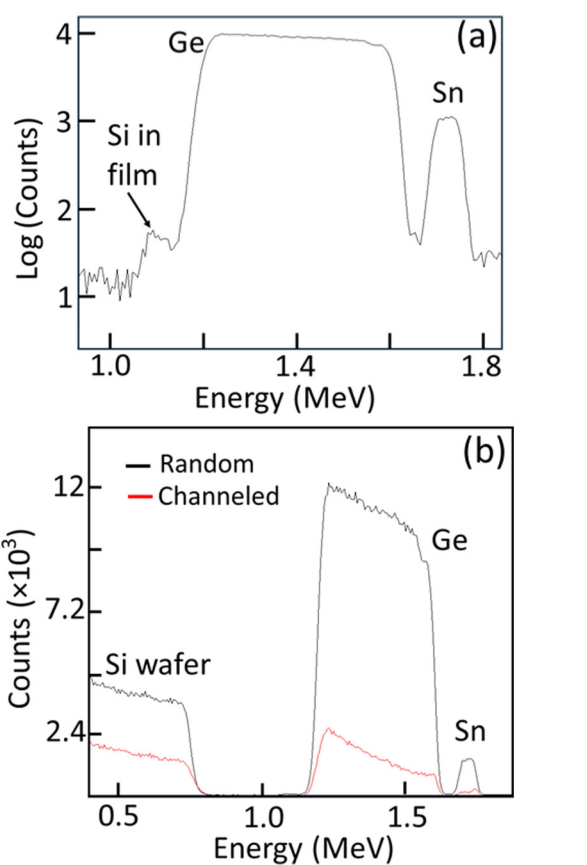


FIG. 1. (a) 2.0 MeV RBS spectrum of Ge_{0.891}Sn_{0.069}Si_{0.046} plotted in a logarithmic scale to enlarge the Si signal. (b) Random RBS (black line) and channeled (red line) spectra of the same sample. The high degree of channeling indicates good crystallinity and complete Sn substitutionality in the Si–Ge lattice.

The Sn content in the $Ge_{1-x-y}Si_xSn_y$ samples in Table I is increased from 5.5% to 11% as the growth temperature is lowered from 200 to 160 °C. This trend aligns with the expected compositional dependence behavior in this class of materials, namely, progressively lower temperatures required for full Sn substitution lead to higher Sn contents in the lattice. Additionally, the table indicates that decreasing the growth temperature also reduces the growth rate, which limits the overall thickness of the resultant layers as shown in the last column. This reduction in the thickness may also be attributed to a concomitant increase of the strain differential between Ge and $Ge_{1-x-y}Si_xSn_y$ as the Sn content increases with decreasing temperature. We observe that under these temperature conditions the incorporation of Si in the crystal decreases by half. This is likely due to the reduced reactivity of Si₄H₁₀ relative to SnH₄ and GeH₃Cl at lower temperatures, limiting its efficiency as a source of Si.

Since the film Si content is low and its corresponding RBS signal is weak and located at the edge of the strong Ge contribution, we conducted XPS experiments to corroborate the Si incorporation and composition. The experiments were conducted in a Kratos Axis Supra+ instrument using the Al K_{α} line at 1486.6 eV. Depth profiling was performed by collecting spectra after subjecting the film to a 25-s Ar+ sputtering step between each collection, which translate to a depth variation of about 20 nm. The red and green plots in Fig. 2 correspond to representative spectra from sample 1 in the table, illustrating the Sn peaks in the main panel and Si peaks in the inset. The Sn signals are smooth curves, while Si are slightly noisy but still well-defined, unambiguously illustrating the presence of Si throughout the layer. The integrated peak intensities from the red plots yielded 4.93% Si, 5.44% Sn, and 89.63% Ge, while those of the green plots yielded 5.12% Si, 5.52%

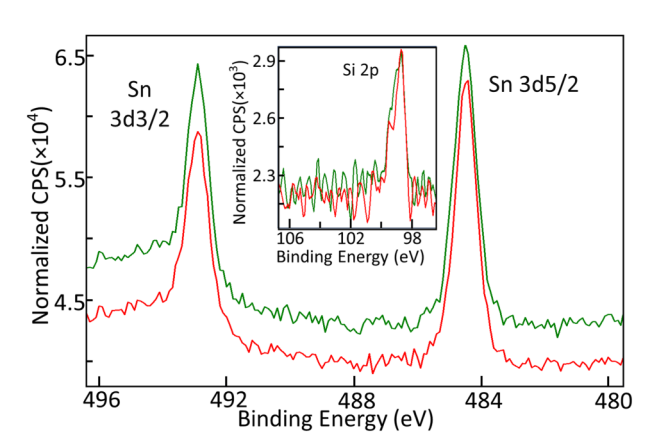


FIG. 2. Green and red plots represent two XPS spectra collected from the Ge_{0.895}Sn_{0.055}Si_{0.05} film. These were obtained after consecutive 25-s sputtering intervals, with the green plot showing a spectrum after first interval and the red one after a second interval. The main panel compares the Sn signals from the spectra. The peak shape and intensity are nearly identical but they are slightly offset for differentiation. The inset shows a near perfect overlap of the Si signals, indicating closely matched compositions. Quantifications of the Sn and Si signals were performed to obtain stoichiometry of the sample using instrument-specific sensitivity factors.

Sn, and 89.36% Ge. The very similar concentrations at the two locations are consistent with the flat RBS compositional profiles assumed to fit the RBS spectra and confirm the Ge_{0.895}Sn_{0.055}Si_{0.05} stoichiometry measured by RBS, including the Si concentration.

The epitaxial films are tetragonally distorted due to the epitaxial stress, with an in-plane lattice parameter a and perpendicular lattice parameter c. HRXRD was employed to determine these lattice constants. The measurements were performed at room temperature using a Panalytical X'Pert Pro MRD system based on Cu $K\alpha_1$ radiation. We start by aligning the sample to the Si (004) Bragg reflection, and from there, the position of the film (004) peaks is measured. This gives the lattice parameter c. Next, we measure (224) reciprocal space maps (RSMs) from which we extract both the a and c lattice parameters. The relaxed cubic lattice constant a_0 is obtained from a and c using standard elasticity theory.³² The strain is defined as $\epsilon = (a - a_0)/a_0$.

Figure 3 shows on-axis XRD plots with strong, sharp (004) Bragg reflections for the epilayer and buffer for sample 2. The interference fringes on both sides of the $Ge_{1-x-y}Si_xSn_y$ (004) peak indicate a sharp interface with Ge. The inset of the figure presents (224) RSMs corresponding to Ge and $Ge_{1-x-y}Si_xSn_y$. These maps exhibit narrow and symmetrical profiles consistent with superior crystallinity of the layers. Note that the $Ge_{1-x-y}Si_xSn_y$ (224) peak falls below the relaxation line (indicated by the red line in figure) and is vertically aligned with the Ge peak along the pseudomorphic direction, indicating that the epilayer is biaxially strained to the buffer, as expected for a tetragonal distortion from cubic symmetry. The horizontal and vertical lattice parameters of the distorted lattice were measured to be a = 5.667 Å and c = 5.728 Å, respectively. From these values, we obtain $a_0 = 5.7024 \,\text{Å}$. This yields a strain value $\epsilon = -0.6051\%$. From the above strain definition, a negative value indicates compressive strain. Using Vegard's law and

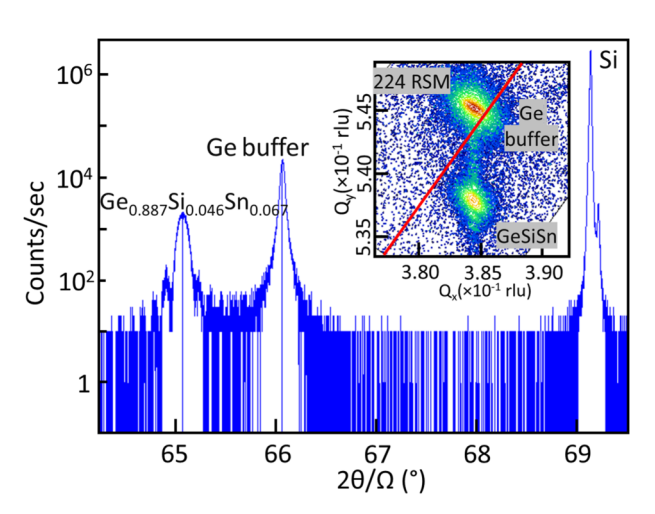


FIG. 3. XRD plots showing 004 peaks (blue line) and (224) RSM (inset) for \sim 6.7% Sn, 4.6% Si sample grown on a Ge buffer. The relaxation line passes slightly below the buffer peak indicating a slight tensile strain. The Ge_{1-x-v}Si_xSn_v (224) peak lies below the relaxation line and aligns with the Ge peak in the vertical direction, indicating pseudomorphic growth.

adopting the RBS Si concentration of 4.6%, the Sn content is calculated to be 6.7% for this sample. Note that the common in-plane parameter of Ge and $Ge_{1,x-y}Si_xSn_y$, a = 5.667 Å, is larger than the bulk Ge value $a = 5.657 \,\text{Å}$. This discrepancy is attributed to the slight tensile strain induced in Ge during growth on the thermally mismatched Si.

HRXRD analyses of all samples in Table I provided their relaxed lattice constants, strain values, and Sn concentrations. The latter were in good agreement with direct RBS measurements but systematically slightly larger, supporting the claim that the Sn measured by RBS in these samples is fully substitutional. The table shows a monotonic increase of the relaxed lattice parameter and strain magnitude with increasing Sn content, as expected.

All samples in this study are compressively strained. No relaxation was observed in any of the films, regardless of composition and thickness. We note that strained structures of Ge_{1-v}Sn_v binary alloys are routinely produced by molecular beam epitaxy (MBE) on Ge wafers and Ge-buffered Si wafers. The ultralow temperature and pressure conditions of this technique promote the integration of lattice-coherent layers which have been utilized to study fundamental properties and demonstrate device applications. For instance, MBE-grown strained films of $Ge_{1-\nu}Sn_{\nu}$ have been reported to serve as channel materials in MOSFET due to their higher hole mobility. 33,34 A key advantage of our strained $Ge_{1-x-y}Si_xSn_y$ samples over $Ge_{1-\nu}Sn_{\nu}$ is the ability to controllably add small amounts of Si whose incorporation allows for fine-tuning of optical and electrical properties as well as strain states, providing additional flexibility in device design.

Further structural characterizations were conducted using STEM. Figure 4(a) shows a phase contrast image of the 5.5% Sn and 5% Si alloy sample 1 in Table I acquired in the scanning mode (STEM) with a JEOL ARM200F microscope. The image highlights the excellent crystallinity and morphology observed in these samples. The $Ge_{1-x-y}Si_xSn_y$ top layer is uniform, monocrystalline, and defect-free as expected due to the pseudomorphic integration onto the Ge buffer layer, as shown by the high-resolution image in the inset that reveals a sharp, epitaxial interface between the film and the Ge buffer. The surface profile of the film is planar within the field of view. AFM examinations corroborated the flat morphology as shown in Fig. 4(b) which displays an AFM image of the same sample. The surface is smooth throughout and lacks cross hatch patterns typical for relaxed Ge1-vSnv layers grown on Ge buffers. 18,35 The AFM RMS roughness is 0.7 nm, which is typical for these fully strained samples. Additionally, Nomarski optical images confirmed the flat surface morphology extends over larger areas.

Extensive TEM characterizations were conducted on a set of four samples with varying stoichiometries as listed in the table to fully assess the crystallinity of these materials. Figure 5 shows images of a film with a Ge_{0.895}Si_{0.025}Sn_{0.08} composition and a thickness of 55 nm grown upon a 600 nm Ge buffer. The main panel image displays the entire thickness profile of the film, highlighting the lack of defects as expected due to the pseudomorphic growth. The inset presents a high-resolution image of the interface between Ge and the strained epilayer revealing the defect-free epitaxial relationship and the full commensuration of the (111) lattice fringes. The TEM-measured layer thickness is 60 nm, close to the 55 nm

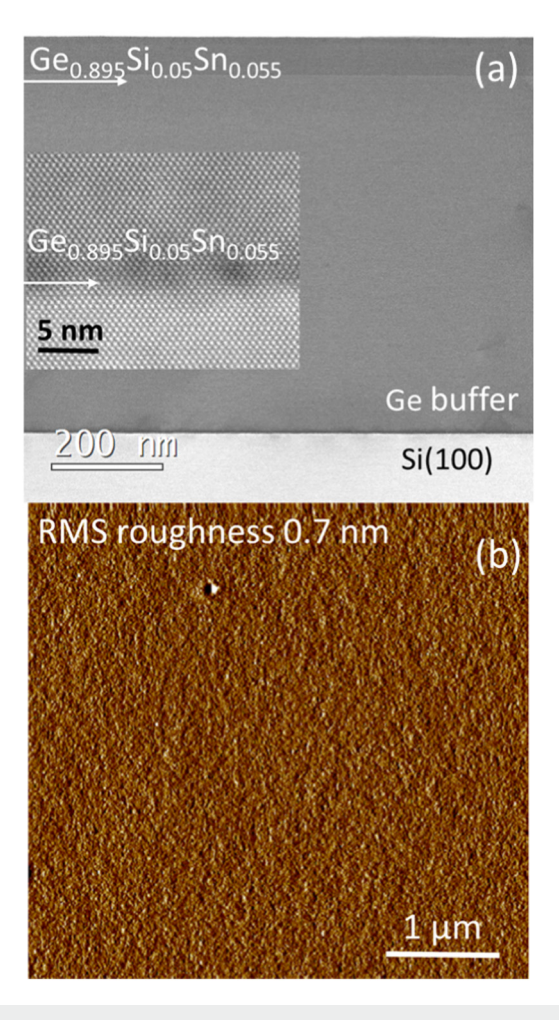


FIG. 4. (a) Bright field STEM image of the 70 nm thick Ge_{0.895}Si_{0.05}Sn_{0.055} film grown on the 700 nm thick, Ge buffer. The top layer is flat and crystalline. The inset shows a high-resolution view of the interface between the film and the buffer. (b) AFM image of the same sample showing a smooth surface with very low RMS roughness of 0.7 nm.

obtained by RBS. In all cases, the microstructure consistently resembled the one shown in Fig. 5, irrespective of the Sn concentration and the film thickness.

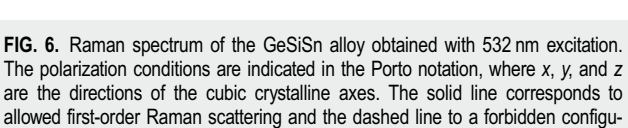
B. Raman studies

Raman spectra were obtained for some of the $Ge_{1-x-y}Si_xSn_y$ films described above to further investigate bonding properties of these materials. In particular, the atomic distribution in the average diamond lattice may deviate from randomness depending on the particular method of synthesis and on the chemical precursors used for the growth. The observation of an interaction between the presence of Si and the incorporation of Sn suggests that such deviations are possible, and Raman studies provide a tool to investigate them.

Ge-Ge

Counts (arbitrary scale

Ge{0.891}Si_{0.046}Sn_{0.063}



ration. The low-energy peak at 282 cm⁻¹, quite apparent in the "forbidden" spec-

trum, is a two-phonon feature that is also observed in pure Ge.

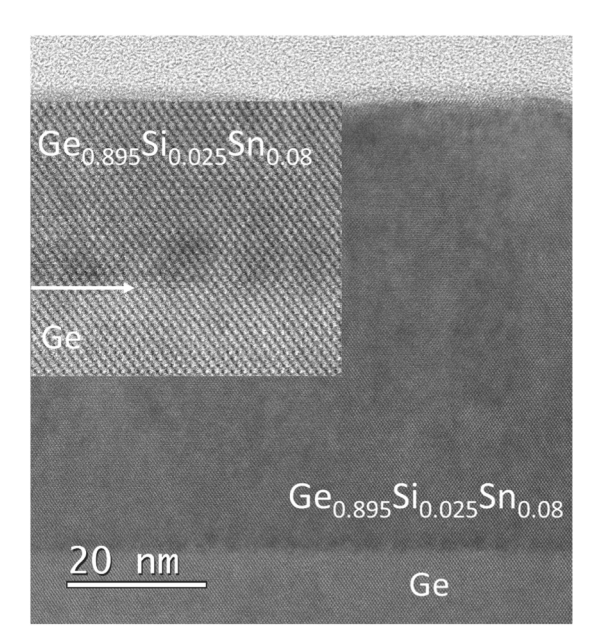


FIG. 5. STEM bright field image of the \sim 60 nm thick Ge_{0.895}Si_{0.025}Sn_{0.025}Sn_{0.08} film grown on the Ge buffer. The inset shows a high-resolution image of the interface between the epilayer and the Ge buffer.

The Raman spectra were collected in the backscattering configuration in a custom micro-Raman setup using 1.3 mW of 532 nm illumination. The laser light was focused on the sample using a 100× objective and the scattered light collected with a standard CCD detector. The Raman shifts in the alloys were carefully calibrated by also measuring bulk Ge and Si samples and rescaling the results so that the peaks agree with high accuracy measurements from Trzeciakowski and co-workers, which imply $\omega_{\rm Si} = 520.69~{\rm cm}^{-1}$ and $\omega_{\rm Ge} = 300.265~{\rm cm}^{-1}$ at room temperature. Spikes in the collected spectra were removed using a custom variant of the Katsumoto–Ozaki algorithm, in which we combine binomial smoothing with Savitzky–Golay smoothing.

Figure 6 shows a typical Raman spectrum from one of the ternary samples. For the chosen backscattering configuration, the spectrum consists of longitudinal optical vibrations. The superb crystalline quality is demonstrated by the excellent depolarization ratio, in full accordance with the selection rules for diamondstructure materials. The Raman spectrum from ternary $Ge_{1-x-y}Si_xSn_y$ alloys was first studied by D'Costa and co-workers.³ For relatively modest Si and Sn concentrations, it is quite similar to the Raman spectrum of Ge-rich SiGe alloys, dominated by two peaks that are informally referred to as "Ge-Ge" and "Si-Ge" vibrations. "Si-Sn" vibrations may also contribute to the Raman spectrum, but they overlap in frequency with the Si-Ge modes, since Si is much lighter than Ge or Sn and the Raman frequency is approximately proportional to $\mu^{-1/2}$, where μ is the reduced mass of the two atoms.³⁹ The intensities of these peaks are roughly proportional to the fraction of Ge-Ge and Si-Ge bonds in the sample. We see clear evidence for Ge-Ge and Si-Ge modes in Fig. 6, but the

latter is much weaker on due to low Si concentrations. This also explains why no Si–Si Raman peak is observed.

Alloy Raman peaks have a characteristic asymmetric profile, and the frequency of a mode is phenomenologically defined as the maximum of its Raman peak. For the Si–Ge mode, this frequency has a complicated compositional dependence, but the Ge–Ge mode frequency is a linear function of *x* and *y* that lends itself to characterization work, including composition determinations. Accordingly, we focus our analysis on this peak, which is shown in more detail and compared with the Raman peak of Ge in Fig. 7.

To account for the asymmetric profile, we fit our Raman peaks with an exponentially modified Gaussian (EMG) lineshape, ³⁸ from which we extract the peak maxima. D'Costa and co-workers proposed a compositional dependence of the LO mode frequency given by

$$\omega_{\text{Ge-Ge}}(x,y) = \omega_0^{\text{Ge}} - \alpha_{\text{Ge-Ge}}^{\text{GeSi}} x - \alpha_{\text{Ge-Ge}}^{\text{GeSn}} y + b_{\text{Ge-Ge}} \epsilon(x,y).$$
 (3)

In the last term in Eq. (3), $\epsilon(x,y)$, is the strain that appears in Table I. For a tetragonal distortion, the strain coefficient is given by $b_{\text{Ge-Ge}} = \frac{1}{\omega_{\text{Ge-Ge}}} \left[q - p \left(\frac{C_{12}}{C_{11}} \right) \right]$, where C_{11} and C_{12} are elastic constants, and we use the notation p, q, r for the three symmetry-allowed anharmonic coefficients in the diamond structure. Using this notation, the Grüneisen parameter for the mode, defined as $\gamma = -\partial \ln \omega_{\text{Ge-Ge}}/\partial \ln V$, is given by $\gamma = -(p+2q)/6\omega_{\text{Ge-Ge}}^2$.



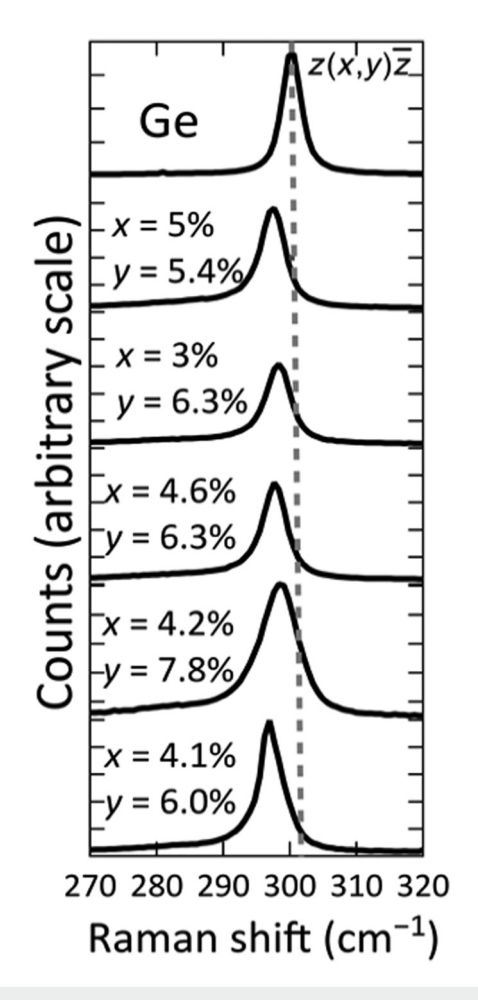


FIG. 7. Allowed $z(x, y)\overline{z}$ Raman spectra from selected chlorogermane GeSiSn samples around the frequency corresponding to the Ge-Ge mode.

D'Costa et al. used $b_{Ge-Ge} = -415 \text{ cm}^{-1}$ based on p and q values for pure Ge from a classic paper by Cerdeira et al. 41 These values, however, lead to $\gamma = 0.88$, considerable less than the experimental value $\gamma = 1.00$ (Ref. 42). In more recent direct Raman measurements on epitaxially strained Ge1-xSix epitaxial films, Reparaz et al. found $b_{\rm Ge-Ge} = -(460 \pm 20) \ {\rm cm}^{-1}$ for pure Ge, in much better agreement with the experimental Grüneisen parameter.⁴³ They also found a very weak dependence on composition for $b_{\mathrm{Ge-Ge}}$, justifying the use of a single constant in Eq. (3). Very similar results $(b_{\mathrm{Ge-Ge}} = -450 \pm 30 \ \mathrm{cm^{-1}}$ for pure Ge) were obtained by Pezzoli and co-workers, who also discuss a theoretical model supporting the very weak compositional dependence.⁴⁴ However, in more recent work, Yokogawa et al.45 claim a stronger strain dependence $(b_{\rm Ge-Ge} \sim -575 \ {\rm cm}^{-1})$. In view of these uncertainties, we decided to carry out our own measurements on pure Ge epitaxial layers grown in our lab and then use the value of b_{Ge-Ge} determined from those measurements to analyze our GeSiSn data. We reasoned that even if Raman strain measurements contain some unknown systematic error

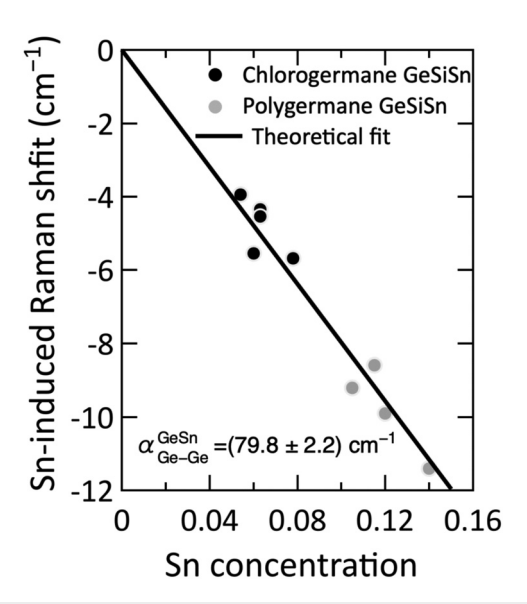


FIG. 8. Sn-dependence $\Delta\omega_{\text{Ge-Ge}}(y)$ of the Ge-Ge mode frequency in GeSiSn alloys. The solid line is a linear fit.

that explains the variations from group to group, this error is likely to cancel out if we use our own strain measurements in pure epitaxial Ge to correct our GeSiSn results for strain, since both sets of data are obtained using the same experimental setup under identical conditions. The value we found was $b_{\text{Ge-Ge}} = -427 \pm 30 \text{ cm}^{-1}$. This is much more consistent with the results from Reparaz et al.⁴³ and 8 Pezzoli et al.,44 than with Yokogawa et al.45

D'Costa and co-workers performed a two-dimensional adjustment of Eq. (3) to their experimental data so that the two linear coefficients $\alpha_{\rm Ge-Ge}^{\rm GeSi}$ and $\alpha_{\rm Ge-Ge}^{\rm GeSn}$ could be extracted from the fit. Their main purpose was to verify the conjecture that these coefficients should be "transferable" from the binary alloys Ge_{1-x}Si_x and $Ge_{1-y}Sn_y$ to the ternary $Ge_{1-x-y}Si_xSn_y$. The conjecture turned out to be correct within experimental error. However, since $\alpha_{\text{Ge-Ge}}^{\text{GeSi}}$ is about four times smaller than $\alpha_{\rm Ge-Ge}^{\rm GeSn}$, Si concentrations approaching at least 20% are needed for the fits to converge well. These are much higher than the Si concentrations in the present paper. Furthermore, our main interest here is to assess the structural properties of Ge_{1-x-v}Si_xSn_v alloys synthesized with GeH₃Cl compared to ternaries grown using the more traditional polygermane route (Ge₄H₁₀ and Ge₃H₈). For this purpose, we simply subtract the strain shift and the Si-induced shift using the value $\alpha_{\rm Ge-Ge}^{\rm GeSi}=17.1~{\rm cm}^{-1}$ from D'Costa et al. and consider only the Sn-concentration dependence of the Raman frequencies $\Delta\omega_{\text{Ge-Ge}}(y) = \omega_{\text{Ge-Ge}}(x, y) + \alpha_{\text{Ge-Ge}}^{\text{GeSi}}(x - b_{\text{Ge-Ge}}\boldsymbol{\epsilon}(x, y) - \omega_0^{\text{Ge}}.$

Figure 8 shows $\Delta\omega_{\text{Ge-Ge}}(y)$ for selected ternary alloys grown with GeH₃Cl and for other ternary alloys grown with polygermanes. We see that the data are consistent with a linear y-dependence and that there seems to be no distinction between the two synthetic approaches to GeSiSn alloys, corroborating the conclusion that the GeH₃Cl route leads to completely

TABLE II. Representative $Ge_{1-\nu}Sn_{\nu}$ (y = 0.022-0.70) samples grown on Ge buffers between 230 and 175 °C. Sample properties, including film thicknesses, Sn concentrations (determined from RBS and XRD), relaxed lattice parameters (a₀), and strains (ε) are listed.

Sample	Tg (°C)	XRD Sn (%)	RBS Sn (%)	ε (%)	a ₀ (Å)	Thickness (nm)
1	230	2.1	2.2	-0.1382	5.674	66
2	210	3.2	3.2	-0.3338	5.684	52
3	195	3.9	3.9	-0.4379	5.6892	29
4	175	7.5	7.0	-0.9461	5.7198	28

equivalent materials. A fit of the y-dependence with the expression $-\alpha_{\text{Ge-Ge}}^{\text{GeSn}}y$ gives $\alpha_{\text{Ge-Ge}}^{\text{GeSn}}=(79.8\pm2.2)~\text{cm}^{-1}$, somewhat below $\alpha_{\text{Ge-Ge}}$ gives $\alpha_{\text{Ge-Ge}} = (7.3 \pm 2.2) \text{ cm}^{-1}$, the published values $\alpha_{\text{Ge-Ge}}^{\text{GeSn}} = (94. \pm 2.2) \text{ cm}^{-1}$ (Ref. 38), $\alpha_{\text{Ge-Ge}}^{\text{GeSn}} = (94.0 \pm 7.1) \text{ cm}^{-1}$ (Ref. 46), and $\alpha_{\text{Ge-Ge}}^{\text{GeSn}} = (89.9 \pm 2.9) \text{ cm}^{-1}$ (Ref. 47), but in even better agreement with the transferability conjecture in Ref. 38, since the corresponding measurement in binary $Ge_{1-y}Sn_y$ alloys gives $\alpha_{Ge-Ge}^{GeSn} = (75.4 \pm 4.5) \text{ cm}^{-1}$ (Ref. 48).

C. Growth of $Ge_{1-y}Sn_y$ alloys on the Ge buffers and bare Si wafers via GeH₃Cl

Our previous work with GeH₃Cl demonstrated its potential as a CVD precursor for fabricating Ge epitaxial layers on Si and photodiode devices.²⁹ We also conducted proof of concept experiments aimed at synthesizing Ge_{1-y}Sn_y via reactions of GeClH₃ with SnD₄ at ultralow temperatures (T < 200 °C) using the GSME method. Initial results indicated that dilute amounts of Sn (up to 2%) were incorporated into Ge, as evidenced by XRD.²⁷ In this present study, we expanded our efforts to produce a set of $Ge_{1-\nu}Sn_{\nu}$ films with a wide range of alloy compositions and to characterize their materials properties in detail. The synthesis of $Ge_{1-y}Sn_y$ was conducted on both Ge buffers and on pristine Si wafers through reactions of GeH₃Cl and SnH₄, following the same methods used for the above $Ge_{1-x-y}Si_xSn_y$ on Ge samples. An objective was to test the limits of GeH₃Cl for the synthesis of $Ge_{1-\nu}Sn_{\nu}$ binaries under experimental conditions similar to the ones employed above for the ternaries and compare results between the two systems.

For each run, the substrates were chemically cleaned and placed in the GSME chamber, where they were degassed on the wafer stage prior to growth. Pure GeH3Cl vapor was introduced first into the chamber followed by gaseous SnH4 without a carrier gas. The reactant pressure was adjusted between 4.5×10^{-5} and 7×10^{-5} Torr and the temperature varied from 230 to 175 °C, allowing for an increase in Sn contents from 2.1% to 7.5%. Under these conditions, we produced films with smooth mirrorlike surfaces on both Ge buffers and on Si wafers. Extensive characterizations were performed to assess the material properties. Table II lists the growth temperatures, compositions, lattice constants, strain states, and layer thicknesses for selected samples.

The Sn content and thickness of the Ge_{1-y}Sn_y films were determined by RBS. Ion channeling was employed to examine the epitaxial alignment and evaluate bulk crystallinity. Backscattering intensity profiles of the aligned spectra were obtained, resembling those in Fig. 1(b) above, indicating the presence of monocrystalline

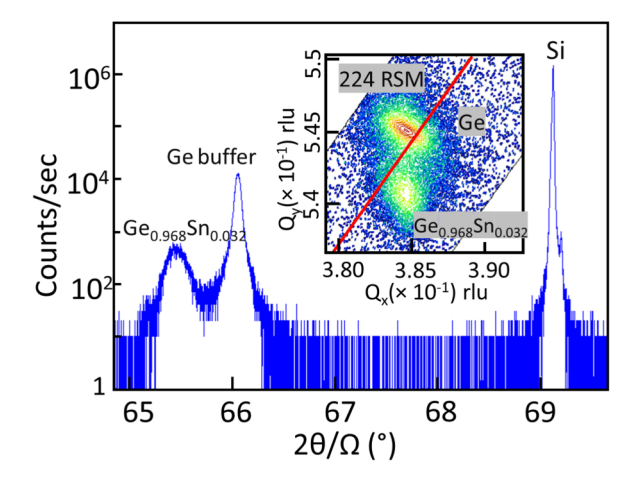


FIG. 9. XRD spectra of Ge_{0.968}Sn_{0.032} grown on Ge. The main panel displays on-axis plot (blue trace) showing (004) peaks. The inset shows (224) RSM of same material. The relaxation line (red) in the RSM passes below the Ge peak, indicating a residual tensile strain in the buffer layer. The Ge_{0.968}Sn_{0.032} peak aligns with the Ge peak in the vertical direction, indicating identical in-plane lattice parameters.

layers with low-defectivity and fully substitutional Sn contents. HRXRD measurements corroborated the RBS compositions and revealed that all films grown on Ge are pseudomorphic and compressively strained. Figure 9 presents the XRD plots for a 3.2% Sn entire distribution of the table (sample 2). The second row of the table (sample 2). on-axis plot (blue line) shows sharp (004) peaks for Ge_{0.968}Sn_{0.032} and Ge, indicating good crystallinity and epitaxial alignment along the growth direction. The corresponding (224) RSM plots are 8 included in the inset. The peaks align well along the vertical direction indicating that $Ge_{0.968}Sn_{0.032}$ is lattice-matched to Ge within the plane of growth and fully strained to the buffer layer. The in-plane (a) and vertical (c) lattice parameters for all films in this study were determined from RSM plots and used to calculate the cubic parameters (a_0) listed in Table II. Sn contents were then obtained using Vegard's law and the values correlate well with RBS results, showing good agreement between the two techniques.

STEM images for the 2.1% Sn film described in the first row of the table are shown in Fig. 10. Figure 10(a) illustrates the full epilayer profile, showing no sign of defects, as expected due to the pseudomorphic nature of the crystal. Additionally, no evidence of Sn segregation is observed, corroborating the single-phase character of the alloy. Figure 10(b) presents a high-resolution image of the interface region between the epilayer and the buffer. The in-plane lattice-matching in this case ensures a sharp and uniform heterojunction that is devoid of defects and exhibits fully commensurate (111) lattice fringes. The TEM images also show that the free surface is slightly etched. This etching occurred during thinning the layer with a focused ions beam to fabricate electron transparent specimens for TEM experiments and does not represent the original surface of the layer.

The above results show that $Ge_{1-y}Sn_y$ films were grown fully strained to Ge, but with reduced Sn compositions ranging from

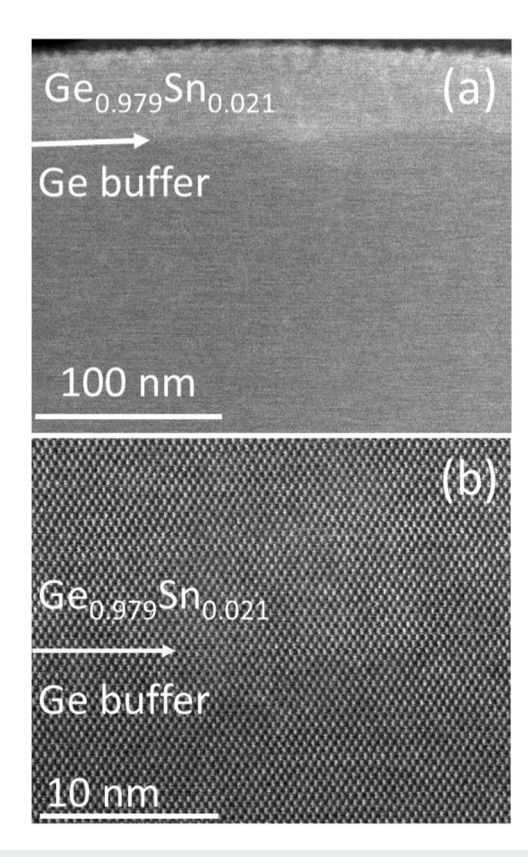


FIG. 10. (a) STEM images of a 66 nm thick Ge_{0.979}Sn_{0.021} layer on a Ge buffer. (b) High-resolution image of the interface between the two materials.

 \sim 2% to 7% and significantly lower thicknesses relative to $Ge_{1-x-y}Si_xSn_y$ (see Table II). This observation promoted further exploration of the growth behavior of $Ge_{1-y}Sn_y$ using the GeH_3Cl method, bypassing the GeH_3Cl method, bypassing

TABLE III. Ge_{1-y}Sn_y (y = 0.03–0.73) samples grown directly on Si between 200 and 173 °C. Growth temperatures (T_g), RBS/XRD Sn concentrations, relaxed lattice parameters (a_0), strains (ε), and film thicknesses are listed.

Sample	<i>T_g</i> (°C)	XRD Sn (%)	RBS Sn (%)	ε (%)	a ₀ (Å)	Thickness (nm)
1	200	2.5	3	-0.1706	5.6778	48
2	197	3.1	3.6	-0.1208	5.6829	69
3	192	3.9	4.3	-0.0471	5.6899	35
4	173	7.2	7.3	-0.4546	5.7188	27

A series of $Ge_{1-y}Sn_y$ samples with mirrorlike surfaces were produced directly on Si and their material properties were determined. A summary of representative films is listed in Table III along with relevant characterizations results. The data show that the Sn concentrations increase from 2.4% to 7.2% as the temperature decreases from 200 to 170 °C, in analogy to layers grown on Ge buffers. A notable distinction is that the XRD-derived Sn contents are slightly lower than those measured by RBS. The discrepancy is largest for the first two samples and diminishes with decreasing temperature, as is apparent from the closely matched XRD/RBS Sn contents of the fourth sample. While the $Ge_{1-y}Sn_y$ samples on Ge are fully strained, the samples on Si are mostly relaxed, as expected, exhibiting residual compressive strains that depend on composition and growth temperature.

The crystallinity of the samples, as determined from the width of the x-ray diffraction peaks, was slightly inferior in the samples grown directly on Si as opposed to those grown on Ge buffers. This is due to the mismatch-induced interface defects, whose dislocation cores propagate through the layer, degrading the microstructure. Nevertheless, the films were monocrystalline and epitaxial, indicating that this approach may hold value in technologies requiring direct growth on Si, under very low thermal budgets, using straightforward deposition techniques. Efforts to increase the concentration and the thickness of these samples resulted in nonhomogeneous multiphase materials containing large amounts of interstitial Sn impurities, indicating that only a limited range of $\text{Ge}_{1-y}\text{Sn}_y$ compositions can be achieved using the GeH_3Cl approach at ultralow temperatures.

III. SUMMARY AND CONCLUSIONS

In this paper, we demonstrate the potential of a novel GeH₃Cl $\stackrel{8}{5}$ precursor to replace higher-order germanes such as Ge₄H₁₀ and Ge₃H₈ for low-temperature, CMOS-compatible development of Sn/Si-based semiconductors. To highlight its effectiveness, we used CVD to fabricate Ge_{1-x-y}Si_xSn_y epitaxial films on Ge-buffered Si substrates. This process involved interactions of GeH₃Cl with SnH₄ and Si₄H₁₀ between 200 and 160 °C. These ultralow temperature conditions are typically associated with MBE processes for SiGeSn growth using solid-source fluxes. Achieving synthesis of monocrystalline films under these conditions via a purely chemical process based on molecular reactions is unique and represents an advance in crystal growth of group-IV alloys.

The $Ge_{1-x-y}Si_xSn_y$ films were fully strained to Ge buffers, exhibiting Si contents of 3%–5% Si and Sn contents of 5%–11% Sn with thicknesses up to 100 nm. For comparison, $Ge_{1-y}Sn_y$ binaries were also grown on Ge buffers under the same conditions. These films are also fully strained to Ge, however, they contain significantly lower amounts of Sn and have reduced thicknesses relative to the ternaries. We next attempted the growth of $Ge_{1-y}Sn_y$ directly on Si without buffers to mitigate the misfit strain with the intention to promote formation of thicker layers with high Sn contents. The $Ge_{1-y}Sn_y$ films on Si exhibited mostly relaxed strain states, as expected, but their thicknesses and Si contents were low and comparable to those on Ge. Attempts to increase Sn content and thickness beyond a limited range were unsuccessful resulting in multiphase products. The study demonstrates that ternary alloys



produced via the GeH_3Cl method can incorporate much higher Sn contents than binary analogs regardless of strain. This suggests that the small Si atoms might compensate for the large Ge–Sn mismatch by lowering bond strains in $Ge_{1-x-y}Si_xSn_y$ compared to $Ge_{1-y}Sn_y$. This, in turn, promotes larger thicknesses and induces better crystallinity.

ACKNOWLEDGMENTS

This work was supported by the U.S. National Science Foundation under Grant Nos. DMR-2119583 and DMR-2235447 and by the Air Force Office of Scientific Research under Grant No. FA9550-23-1-0285.

AUTHOR DECLARATIONS

Conflict of Interest

The authors have no conflicts to disclose

Author Contributions

Aixin Zhang: Conceptualization (lead); Data curation (equal); Formal analysis (equal); Investigation (equal); Project administration (lead); Supervision (lead); Validation (equal); Writing – original draft (lead); Writing – review & editing (lead). Dhruve A. Ringwala: Data curation (equal); Formal analysis (equal); Investigation (equal); Validation (equal). Matthew A. Mircovich: Data curation (supporting). Manuel A. Roldan: Data curation (supporting). John Kouvetakis: Conceptualization (lead); Data curation (supporting); Project administration (lead); Supervision (lead); Writing – original draft (lead); Writing – review & editing (lead). José Menéndez: Data curation (equal); Formal analysis (equal); Writing – review & editing (equal).

DATA AVAILABILITY

The data that support the findings of this study are available from the corresponding author upon reasonable request.

REFERENCES

- ¹S. Wirths *et al.*, Nat. Photonics **9**, 88 (2015).
- ²Y. Miao et al., Nanomaterials, 11, 2556 (2021).
- ³V. Reboud et al., Photonics Nanostruct. Fundam. Appl. 58, 101233 (2024).
- ⁴A. Mathur, D. Pal, A. Singh, R. Singh, S. Zollner, and S. Chattopadhyay, J. Vac. Sci. Technol. B 37, 041802 (2019).
- ⁵S. Oguz, Appl. Phys. Lett. **43**, 848 (1983).
- ⁶M. T. Asom, E. A. Fitzgerald, A. R. Kortan, B. Spear, and L. C. Kimerling, Appl. Phys. Lett. **55**, 578 (1989).
- **7**G. He and H. A. Atwater, Phys. Rev. Lett. **79**, 1937 (1997).
- ⁸D. Imbrenda, R. Hickey, R. A. Carrasco, N. S. Fernando, J. VanDerslice, S. Zollner, and J. Kolodzey, Appl. Phys. Lett. 113, 122104 (2018).
- ⁹M. Bauer, J. Taraci, J. Tolle, A. V. G. Chizmeshya, S. Zollner, D. J. Smith, J. Menendez, C. Hu, and J. Kouvetakis, Appl. Phys. Lett. **81**, 2992 (2002).
- ¹⁰M. Bauer, C. Ritter, P. A. Crozier, J. Ren, J. Menendez, G. Wolf, and J. Kouvetakis, Appl. Phys. Lett. 83, 2163 (2003).
- ¹¹B. Vincent et al., Appl. Phys. Lett. **99**, 152103 (2011).
- ¹²G. Grzybowski, R. T. Beeler, L. Jiang, D. J. Smith, J. Kouvetakis, and J. Menéndez, Appl. Phys. Lett. 101, 072105 (2012).
- ¹³C. Xu, R. T. Beeler, G. J. Grzybowski, A. V. Chizmeshya, D. J. Smith, J. Menéndez, and J. Kouvetakis, J. Am. Chem. Soc. 134, 20756 (2012).

- ¹⁴M. A. Mircovich, C. Xu, D. A. Ringwala, C. D. Poweleit, J. Menéndez, and J. Kouvetakis, ACS Appl. Electron. Mater. 3, 3451 (2021).
- ¹⁵H. Zhao et al., Opt. Mater. **149**, 114987 (2024).
- 16P. M. Wallace, C. L. Senaratne, C. Xu, P. E. Sims, J. Kouvetakis, and J. Menéndez, Semicond. Sci. Technol. 32, 025003 (2017).
- ¹⁷C. Xu, T. Hu, D. A. Ringwala, J. Menéndez, and J. Kouvetakis, J. Vac. Sci. Technol. A 39, 063411 (2021).
- ¹⁸L. Jiang, C. Xu, J. D. Gallagher, R. Favaro, T. Aoki, J. Menéndez, and J. Kouvetakis, Chem. Mater. 26, 2522 (2014).
- ¹⁹J. Margetis, S. Amir Ghetmiri, W. Du, B. R. Conley, A. Mosleh, R. A. Soref, G. Sun, L. Domulevicz, H. A. Naseem, Shui-Qing Yu, and J. Tolle, ECS Trans. 64, 711 (2014).
- ²⁰W. Dou et al., Opt. Mater. Express 8, 3220 (2018).
- ²¹B. Claflin, G. J. Grzybowski, M. E. Ware, S. Zollner, and A. M. Kiefer, Front. Mater. 7, 44 (2020).
- ²²S. Assali, J. Nicolas, S. Mukherjee, A. Dijkstra, and O. Moutanabbir, Appl. Phys. Lett. 112, 251903 (2018).
- ²³S. B. Samavedam, M. T. Currie, T. A. Langdo, and E. A. Fitzgerald, Appl. Phys. Lett. 73, 2125 (1998).
- ²⁴H.-C. Luan, D. R. Lim, K. K. Lee, K. M. Chen, J. G. Sandland, K. Wada, and L. C. Kimerling, Appl. Phys. Lett. **75**, 2909 (1999).
- 25 See https://strategicmetalsinvest.com/germanium-prices/ for "Strategic Metals Invest" (2024).
- ²⁶M. Patel and A. K. Karamalidis, Sep. Purif. Technol. **275**, 118981 (2021).
- ²⁷R. Yang, W. Song, S. Rao, J. Tao, D. Wang, H. Cao, and Z. Liu, <u>Materials</u> 16, 5374 (2023).
- ²⁸A. Feltrin and A. Freundlich, Renew. Energy 33, 180 (2008).
- 29 A. Zhang, M. A. Mircovich, D. A. Ringwala, C. D. Poweleit, M. A. Roldan, J. Menéndez, and J. Kouvetakis, J. Mater. Chem. C 10, 13107 (2022).
- 30 J. Xie, A. V. G. Chizmeshya, J. Tolle, V. R. D'Costa, J. Menendez, and J. Kouvetakis, Chem. Mater. 22, 3779 (2010).
- ³¹S. Wirths et al., Thin Solid Films, 557, 183 (2014).
- ³²C. Xu, C. L. Senaratne, R. J. Culbertson, J. Kouvetakis, and J. Menéndez, J. Appl. Phys. **122**, 125702 (2017).
- 33 L. Liu, R. Liang, J. Wang, and J. Xu, J. Appl. Phys. 117, 184501 (2015).
- 34S. Gupta et al., paper presented at the 2012 International Electron Devices Meeting, 2012.
- Meeting, 2012.

 35C. L. Senaratne, J. D. Gallagher, L. Jiang, T. Aoki, D. J. Smith, J. Menéndez, and J. Kouvetakis, J. Appl. Phys. 116, 133509 (2014).
- ³⁶W. Trzeciakowski, J. Martínez-Pastor, and A. Cantarero, J. Appl. Phys. 82, 3976 (1997).
- 37Y. Katsumoto and Y. Ozaki, Appl. Spectrosc. 57, 317 (2003).
- ³⁸V. R. D'Costa, J. Tolle, C. D. Poweleit, J. Kouvetakis, and J. Menéndez, Phys. Rev. B **76**, 035211 (2007).
- ³⁹J. Tolle, A. V. G. Chizmeshya, Y. Y. Fang, J. Kouvetakis, V. R. D'Costa, C. W. Hu, J. Menéndez, and I. S. T. Tsong, Appl. Phys. Lett. 89, 231924 (2006).
- ⁴⁰J. Menéndez, in *Raman Scattering in Materials Science*, edited by W. H. Weber and R. Merlin (Springer, Berlin, 2000), Vol. 42, pp. 55–103.
- ⁴¹F. Cerdeira, C. J. Buchenauer, F. H. Pollak, and M. Cardona, Phys. Rev. B 5, 580 (1972).
- ⁴²C. Ulrich, E. Anastassakis, K. Syassen, A. Debernardi, and M. Cardona, Phys. Rev. Lett. 78, 1283 (1997).
- ⁴³J. S. Reparaz, A. Bernardi, A. R. Goñi, M. I. Alonso, and M. Garriga, Appl. Phys. Lett. **92**, 081909 (2008).
- ⁴⁴F. Pezzoli et al., J. Appl. Phys. **103**, 093521 (2008).
- ⁴⁵R. Yokogawa, K. Takeuchi, T. Murakami, K. Usuda, I. Yonenaga, and A. Ogura, Jpn. J. Appl. Phys. 57, 106601 (2018).
- 46J. H. Fournier-Lupien et al., Appl. Phys. Lett. 103, 263103 (2013).
- ⁴⁷J. Schlipf *et al.*, J. Raman Spectrosc. **52**, 1167 (2021).
- ⁴⁸V. R. D'Costa, J. Tolle, R. Roucka, C. D. Poweleit, J. Kouvetakis, and J. Menéndez, Solid State Commun. 144, 240 (2007).